INNSPUB

**Journal of Biodiversity and Environmental Sciences | JBES**
**ISSN: 2220-6663 (Print); 2222-3045 (Online)**
**Website: https://www.innspub.net**
**E-mail contact: info@innspub.net**
**Vol. 27, Issue: 2, p. 10-20, 2025**

RESEARCH PAPER OPEN ACCESS

# Biogenic fabrication of biochar-functionalized iron oxide nanoparticles using *Miscanthus sinensis* for oxytetracycline removal and toxicological assessment

**Meenakshi Sundaram Sharmila, Gurusamy, Annadurai***

*Sri Paramakalyani Centre of Excellence in Environmental Sciences, Manonmaniam Sundaranar University, Alwarkurichi, Tamil Nadu, India*

**Key words:** BC-$Fe_3O_4$ NPs, *Miscanthus sinensis*, (OTC) removal, Co-precipitation, Photocatalytic degradation

DOI: https://dx.doi.org/10.12692/jbes/27.2.10-20 [ Published: August 07, 2025 ]

**ABSTRACT**

This study reports the green synthesis of biochar-coated iron oxide nanoparticles (BC-$Fe_3O_4$ NPs) using *Miscanthus sinensis*-derived biochar via a co-precipitation method. The resulting BC-$Fe_3O_4$ NPs were thoroughly characterized using X-ray Diffraction (XRD), Fourier Transform Infrared Spectroscopy (FTIR), Scanning Electron Microscopy coupled with Energy-Dispersive X-ray Spectroscopy (SEM-EDX), Thermogravimetric Analysis/Differential Thermal Analysis (TGA/DTA), and Brunauer-Emmett-Teller (BET), which confirmed the successful incorporation of $Fe_3O_4$ onto the biochar matrix, along with enhanced surface functionality and mesoporosity. Photocatalytic degradation tests demonstrated efficient removal of oxytetracycline (OTC), achieving up to 90% degradation within 60 minutes under UV irradiation, with optimal activity observed at mention pH and dosage. Antibacterial assays revealed significant inhibition zones against *Escherichia coli* and *Serratia marcescens*, especially during the initial two hours of treatment. Reusability assessments showed moderate regeneration efficiency across three cycles, whereas zebrafish embryo toxicity tests demonstrated a dose-dependent rise in developmental abnormalities, decreased hatching rates, and increased mortality. Overall, the findings suggest that BC-$Fe_3O_4$ NPs hold promise as an eco-friendly, cost-effective material for water purification, though further investigation into their long-term environmental safety.

***Corresponding Author:** G. Annadurai ✉ gannadurai@msuniv.ac.in

## INTRODUCTION

Oxytetracycline, the most commonly used tetracycline antibiotic in animal husbandry, is poorly absorbed and largely excreted in faeces. Its stable molecular structure resists microbial degradation, allowing it to persist in the environment and contribute to pollution. This approach has emerged as a viable solution for wastewater management, particularly in the context of advancing green technologies (Omer *et al.,* 2022). The urgency is further intensified by the rapid depletion of water reserves, driven by the exponential growth of the global population and the impacts of climate change (Eltaweil *et al.,* 2022).

In biochar/metal oxide composites, the biochar acts as a porous carbon framework that is surface-functionalized with metal oxide, thereby increasing the adsorbent's surface area (Dhila *et al.,* 2025). The biochar (BC) was further modified with manganese and iron (Mn-Fe) to enhance its physicochemical properties and improve its adsorption efficiency for removing $Pb^{2+}$ ions from synthetic wastewater (Ahmed *et al.,* 2021). This study examines the influence of key operational parameters- such as solution pH, initial metal ion concentration, and adsorbent dosage- on the efficiency of $Pb^{2+}$ removal (Shafiq *et al.,* 2025).

Nanobiochar can be synthesized from conventional biochar using various techniques, Mechanical grinding is commonly employed to reduce particle size to the nanoscale. In addition to mechanical approaches, flash heating has been used to directly produce graphitic nanosheets (Oleszczuk *et al.,* 2016). utilized an ultrasonic vibrator to disperse biochar particles, followed by sonication to achieve nanoscale dimensions. Among the reported methods, ball milling has emerged as the most effective and widely preferred technique for nanobiochar production (Shui *et al.,* 2016).

The Fe oxide/biochar nanocomposite (FeBN) was synthesized using the co-precipitation method. In brief, brewery spent grain was pyrolyzed at 350 °C for 3 hours to produce biochar (Pap *et al.,* 2023). This biochar was subsequently impregnated with $FeCl_3{\cdot}6H_2O$ through a co-precipitation process (Jin, Ying-Hui *et al.,* 2020). This approach eliminates the need for high-temperature annealing and enhances the adsorption capacity of the magnetic biochar through the photocatalytic properties of ZnO (Zhang *et al.,* 2020).

In this study, it was hypothesized that a biochar/iron oxide composite could be successfully synthesized using a green method and would exhibit effective methylene blue (MB) removal capabilities. To test this, banana peel biochar was modified with banana peel extract and $FeSO_4$ under ultrasonic treatment at room temperature. The resulting material was characterized, and its adsorption behaviour was evaluated (Ahmaruzzaman *et al.,* 2021).

A Fe oxide/biochar nanocomposite (FeBN) made from brewery spent grain was tested to remove CLR from water. The highest CLR removal happened at pH 6, with a maximum adsorption capacity (qmax) of 7.91 mg/g at 30 °C (Li *et al.,* 2021).

This research presents a sustainable method for synthesizing biochar-coated iron oxide nanoparticles (BC-$Fe_3O_4$ NPs) using biochar derived from *Miscanthus sinensis*, targeting the removal of oxytetracycline (OTC) from aqueous environments (Shafiq *et al.,* 2025). The $Fe_3O_4$ nanoparticles were fabricated via a co-precipitation process and subsequently combined with biochar. Characterization techniques such as XRD, FTIR, SEM, EDX, TGA/DTA, and BET confirmed the successful synthesis and integration of the nanomaterials, highlighting enhanced surface properties and a mesoporous structure. The BC-$Fe_3O_4$ NPs demonstrated notable photocatalytic activity, particularly under neutral pH and higher dosage conditions. These findings support the potential of BC-$Fe_3O_4$ NPs as a cost-effective and environmentally friendly material for wastewater treatment and environmental remediation.

## MATERIALS AND METHODS

### Synthesis of biochar-coated iron oxide nanoparticles (BC-$Fe_3O_4$ NPs)

*Materials*

All chemicals used were of analytical grade and used without further purification. Ferric chloride hexahydrate ($FeCl_3 \cdot 6H_2O$), ferrous sulfate heptahydrate ($FeSO_4 \cdot 7H_2O$), and sodium hydroxide (NaOH) were obtained from Vishnu Priya Chemicals Pvt Ltd. Biochar was prepared from *Miscanthus sinensis* by pyrolysis at in a muffle furnace under 700°C a nitrogen atmosphere (Kumar *et al.*,2022).

*Preparation of biochar*

*Miscanthus sinensis* raw plant was washed, dried at 105°C for 24 h, and pyrolyzed at 700°C for 2 h in a nitrogen environment. The resulting biochar was ground and sieved to a particle size <100 µm. Biochar made from *Miscanthus sinensis* was passed through a sieve to get particles around 75 µm in size. Then, 5 g of this biochar was placed in a 500 mL conical flask with 2 M citric acid and shaken for 24 hours (Tang *et al.,* 2013). After that, the mixture was spin in a centrifuge at 3000 rpm for 10 minutes. The biochar was washed two times with deionized water to remove any leftover acid, dried at 60 °C, and then stored in clean culture tubes for later use.

*Synthesis of $Fe_3O_4$ nanoparticles*

Iron oxide nanoparticles were synthesized the co-precipitation method Scheme 1. shows briefly, $FeCl_3 \cdot 6H_2O$ and $FeSO_4 \cdot 7H_2O$ were mixed in a 2:1 molar ratio in deionized water under nitrogen atmosphere with vigorous stirring at 80°C. Aqueous NaOH (1 M) was added dropwise until the pH reached 10, resulting in the formation of a black precipitate of $Fe_3O_4$ nanoparticles. The precipitate was magnetically separated, washed with deionized water and ethanol, and dried under vacuum at 60°C (El-Abid *et al.,* 2023) (Fig. 1).

*Biochar coating iron oxide nanoparticles*

The dried $Fe_3O_4$ nanoparticles were dispersed in deionized water containing a known amount of biochar (typically 1:1 w/w ratio). The suspension was sonicated for 30 min and then stirred at 60°C for 4 h to allow effective adhesion of biochar onto the nanoparticle surfaces. The coated nanoparticles were magnetically separated, washed with water to remove unbound biochar, and dried under vacuum (Salim *et al.,* 2023).

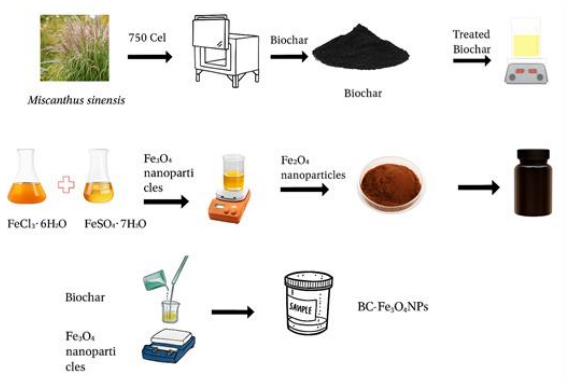


**Fig. 1.** Schematic illustration of (BC-$Fe_3O_4$ NPs) synthesis

*Photocatalytic activity*

The efficiency of BC-$Fe_3O_4$ nanoparticles in removing (OTC) from an aqueous solution was evaluated. To ensure effective removal, 0.5 g of BC-$Fe_3O_4$ nanoparticles was added to 50 mL of a 10 ppm OTC solution in a 100mL vial. The mixture was stirred at room temperature for 25 minutes. At predetermined time intervals, samples were withdrawn from the vial to measure the remaining OTC concentration using a UV spectrophotometer (Akhtar *et al.,* 2014). The percentage of OTC removal was calculated using the following equation:

$$\text{Degradation efficiency} = \frac{C_0 - C}{C_0} \times 100\%$$

where $C_0$ is the initial concentration of OTC and $C$ is the OTC concentration after a specific time.

*Antibacterial activity*

The microorganisms used in this study were isolated from soil and included *Staphylococcus aureus*, *Klebsiella pneumoniae*, *Escherichia coli*, *Bacillus* species, and *Serratia marcescens*.

All bacterial strains were obtained from 24-hour-old cultures. Two oxytetracycline (OTC) adsorption

samples, prepared in water, were analyzed at various time intervals: 15, 30, 45, and 60 minutes. Sterile discs were soaked in these samples and placed on agar plates inoculated with the test microorganisms. Discs containing untreated OTC served as control.

The plates were incubated at 37 °C for 24 hours. Antibacterial activity was assessed by measuring the diameter of the inhibition zones around each disc, with results expressed in millimetres (mm) (Huang *et al.,* 2014).

*Regeneration of BC-$Fe_3O_4$NPs*

To assess the recyclability of BC-Fe3O4 nanoparticles (NPs), a three-cycle regeneration test was conducted at room temperature. After each cycle, the spent adsorbent was separated from the antibiotic solution by centrifugation at 4000 rpm for 15 minutes. The collected BC-Fe3O4 NPs were then washed with 15 mL of ethanol, followed by 20 mL of distilled water, and shaken at 120 rpm for 45 minutes (Saraswathy, and Shaoqin *et al.,* 2014). The regenerated BC-Fe3O4 NPs were dried in a hot air oven for 2 hours and subsequently reused for the removal of OTC. All regeneration experiments were carried out in triplicate.

*Zebrafish embryo toxicity study*

Zebrafish (*Danio rerio*) were maintained in water containing 18 g of ocean salt, 75 g of sodium bicarbonate ($NaHCO_3$), and 8.4 g of calcium sulfate ($CaSO_4$) per 1000 liters. Wild-type zebrafish were cultured under these conditions. Additional experiments were conducted in simulated marine environments. The night before spawning, adult zebrafish were placed in breeding tanks at a male-to-female ratio of 2:1. They were kept under a 12-hour light and 9-hour dark photoperiod. Fertilization occurred within one hour after the lights were turned on the next morning. Viable embryos were collected and incubated in embryo medium. This medium contained 5 mM NaCl, 0.17 mM KCl, 0.33 mM $CaCl_2$, and 0.33 mM $MgSO_4$. The pH was adjusted to 7.2–7.3. The embryos were maintained at a temperature of 28 ± 1°C with adequate dissolved oxygen (Chen *et al.,* 2015). All experimental procedures were approved by the Institutional Animal Ethics Committee at the Sri Paramakalyani Centre for Environmental Sciences, Manonmaniam Sundaranar University, Alwarkurichi. The study followed international guidelines for the care and use of laboratory animals.

## RESULTS AND DISCUSSION

### Scanning electron microscopy-energy-dispersive spectroscopy (SEM-EDX) analysis

Fig. 2 (a), at lower magnification, displays layered, flake-like particles with rough surfaces. This morphology is typical of materials like clay minerals, graphene derivatives, or layered double hydroxides (LDHs). Fig. 2 (b), taken at higher magnification, reveals sharper edges and a lamellar (sheet-like) structure, confirming the flake-like morphology.

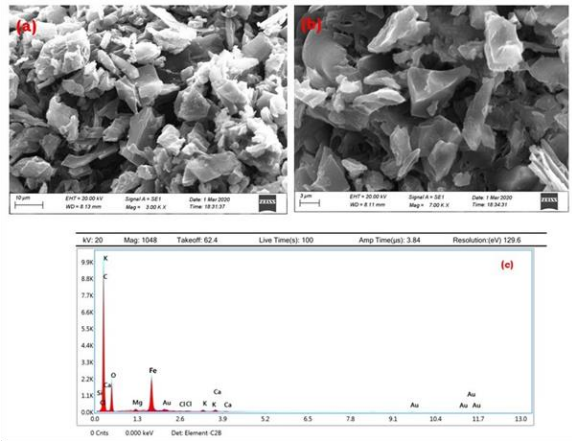


**Fig. 2.** The SEM-EDX image of (a) &(b) BC-Fe3O4 NPs and (c) EDX analysis (BC-Fe3O4 NPs)

Fig. 2 (c) presents the EDX spectrum. It shows a high-intensity carbon (C) peak, indicating a carbon-rich structure, such as biochar. Oxygen (O) is also present, which is common in oxides or hydroxylated surfaces. Potassium (K), calcium (Ca), and magnesium (Mg) suggest the presence of mineral impurities. Iron (Fe) may be from iron oxides or natural contamination. Chlorine (Cl) might have been introduced during synthesis or sample preparation. Scandium (Sc) appears in trace amounts and may be a contaminant or analytical artifact, needing further verification. Overall, the

SEM and EDX results show that the material has a flake-like, layered structure. Its composition is mainly carbon and oxygen, with iron oxides and minor mineral components (Xie *et al.*, 2022).

**X-Ray diffraction (XRD) analysis**

The biochar pattern displays a broad, intense peak centered around 2θ ≈ 23–30°, indicating an amorphous or poorly crystalline structure. This broad hump is typical of carbon-rich biochar due to disordered carbon stacking. In contrast, the $Fe_3O_4$–biochar composite exhibits several sharp peaks between 2θ ≈ 25–50°, indicating the presence of crystalline phases. These peaks suggest the successful incorporation of iron-based crystalline compounds into the biochar matrix. The XRD pattern of pure $Fe_3O_4$ nanoparticles shows sharp, distinct peaks, confirming their crystalline nature (Mou *et al.*, 2016). Major diffraction peaks appear at 2θ ≈ 30.1°, 35.5°, 43.1°, 53.4°, 57.0°, and 62.6°, corresponding to the (220), (311), (400), (422), (511), and (440) crystal planes, respectively.

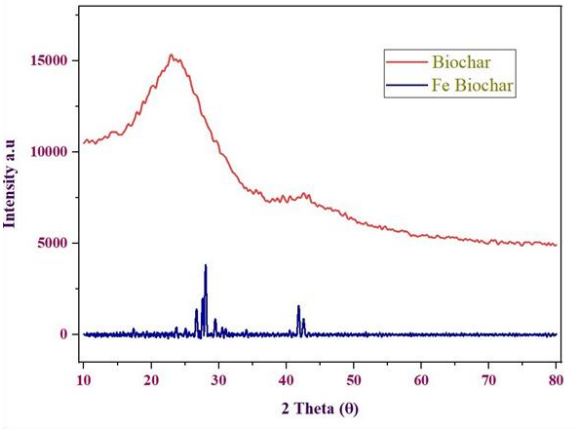


**Fig. 3.** The XRD image of BC-$Fe_3O_4$ nanoparticles

**Thermogravimetric analysis (TGA) and DTA**

Thermogravimetric analysis (TGA) was conducted to assess the thermal stability of BC-$Fe_3O_4$ NPs at a heating rate of 10 °C/min under a gas mixture of 60% nitrogen and 40% air, as shown in Fig. 3. The TGA curve of the biochar displayed a two-step weight loss of approximately 11% upon heating from room temperature to 750 °C. An initial minor weight loss of about 0.343 mg at 66.0 °C corresponds to moisture evaporation. A more significant mass loss between 112.8 °C and 184.8 °C (8.573 mg and 8.229 mg) indicates the decomposition of volatile organic components. Further weight losses from 374.4 °C to 598.2 °C (7.769 mg, 6.937 mg, and 5.112 mg) suggest the progressive thermal degradation or combustion of the residual material.

The DTA curve shows both endothermic and exothermic events. An endothermic peak appears at 177.7 °C (−25.43 µV), which may be due to dehydration or melting (Ntoutoume *et al.*, 2016). After that, an exothermic peak is seen at 257.7 °C (61.237 µV), possibly caused by oxidation or the start of decomposition. Strong exothermic peaks are observed at 336.79 °C (130.244 µV), 468.47 °C (190.48 µV), and 606.33 °C (120.95 µV). These peaks suggest major decomposition or combustion processes. Moisture is lost below 100 °C. In Fig. 4 shows major decomposition happens between about 100 °C and 600 °C in several stages. The exothermic peaks confirm chemical changes like oxidation and decomposition.

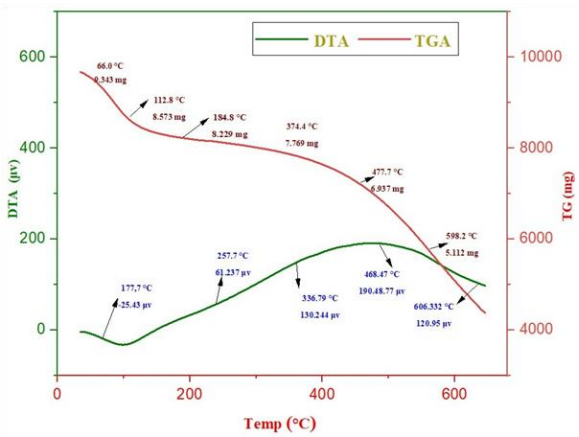


**Fig. 4.** Thermogravimetric analysis (TGA)

**Fourier transforms infrared spectroscopy (FTIR)**

FT-IR spectra of biochar and BC-$Fe_3O_4$ were recorded in the range 4000–400 $cm^{-1}$ to identify functional groups involved in nanoparticle capping and stabilization (Fig. 5). The spectrum of pristine biochar shows a broad band at 3400.56 $cm^{-1}$, corresponding to O–H stretching of hydroxyl groups, and a peak at 2906.17 $cm^{-1}$ due to aliphatic C–H stretching. The band

at 1400.58 $cm^{-1}$ is assigned to aromatic C=C stretching, while the peak at 1200.36 $cm^{-1}$ is attributed to C–O stretching from carboxylic acids, esters, or ethers. Following $Fe_3O_4$ modification, notable spectral changes occur. The O–H band shifts to 3407.23 $cm^{-1}$ with reduced intensity, suggesting interaction with $Fe_3O_4$. The C–H band shifts to 2923 $cm^{-1}$, and a new peak at 1583.34 $cm^{-1}$ appears, corresponding to C=O stretching of carboxyl groups stabilized by iron. A band at 1349.24 $cm^{-1}$ may indicate C–H bending or C–N stretching, reflecting structural reorganization (Abruzzo *et al.,* 2016). The peak at 1074 $cm^{-1}$ is ascribed to C–O or Fe–O stretching, and a distinct signal at 473 $cm^{-1}$ confirms $Fe_3O_4$ deposition.

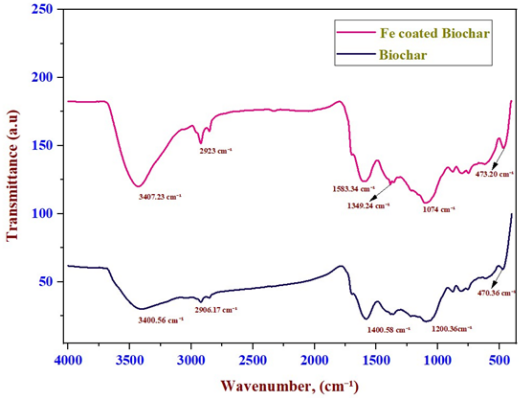


**Fig. 5.** The FTIR image of BC-$Fe_3O_4$

| Wavenumber ($cm^{-1}$) | Functional group | Sample |
|---|---|---|
| 3407.23 | O–H stretching (hydroxyl group) | Fe coated biochar |
| 2923.00 | C–H stretching (alkyl group) | Fe coated biochar |
| 1583.34 | C=C stretching (aromatic ring) | Fe coated biochar |
| 1349.24 | C–N stretching (amine group) | Fe coated biochar |
| 1074.00 | C–O stretching (alcohol/ether group) | Fe coated biochar |
| 473.20 | Fe–O vibration (metal-oxygen bond) | Fe coated biochar |
| 3400.56 | O–H stretching (hydroxyl group) | Biochar |
| 2906.17 | C–H stretching (alkyl group) | Biochar |
| 1400.58 | C–C stretching (aromatic ring) | Biochar |
| 1200.36 | C–O stretching (alcohol/ether group) | Biochar |
| 470.36 | Possible mineral/metal oxide vibration | Biochar |

**Brunauer-emmett-teller analysis (BET)**

The surface area, pore size, and pore volume of BC-$Fe_3O_4$ nanoparticles (NPs) were analyzed using nitrogen adsorption–desorption isotherms at 78.350 K while the Barrett–Joyner–Halenda (BJH) method was applied to measure the pore size. The BC-$Fe_3O_4$ NPs exhibited an average surface area of 3.9466 $m^2/g$ and an average pore diameter of 39.248 nm. These values are attributed to the presence of slit-like pores and a Type II isotherm, which indicates the formation of larger mesopores. In this Fig. 6 shows the suggests that the $Fe_3O_4$ coating altered the biochar's structure, influencing both its surface characteristics and pore architecture (Hazrati *et al.,* 2021). Overall, these structural properties make BC-$Fe_3O_4$ NPs attractive for applications such as catalysis, environmental remediation, and other fields that benefit from high surface area and well-defined porosity.

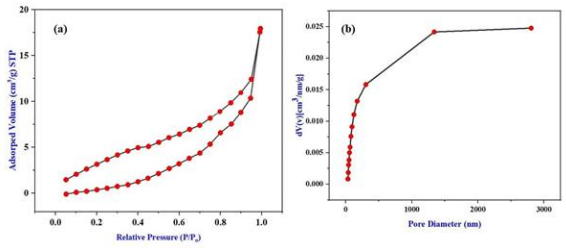


**Fig. 6.** (a) $N_2$ adsorption-desorption isotherms graph and (b) Pore volume distribution of the BC-$Fe_3O_4$ nanoparticles (NPs)

**Photocatalytic activity**

*Mechanism of photocatalytic activity*

The image illustrates the photocatalytic degradation process of pharmaceutical compounds using a biochar/$Fe_3O_4$ composite under UV light. Upon exposure to UV irradiation, electrons in the valence band of the $Fe_3O_4$ nanoparticles are excited to the conduction band, resulting in the formation of electron-hole pairs (Pathy *et al.,* 2023). These charge carriers interact with oxygen ($O_2$) and water ($H_2O$) molecules present in the surrounding environment, leading to the generation of reactive oxygen species (ROS) such as superoxide radicals ($O_2^-$) and hydroxyl radicals (•OH). These ROS play a crucial role in degrading pharmaceutical pollutants depicted in the image by a red-white capsule and a chemical structure by breaking down the complex molecules into simpler, non-toxic byproducts. This mechanism demonstrates the effectiveness of biochar/$Fe_3O_4$

composites in environmental remediation through photocatalytic degradation (Fig. 7).

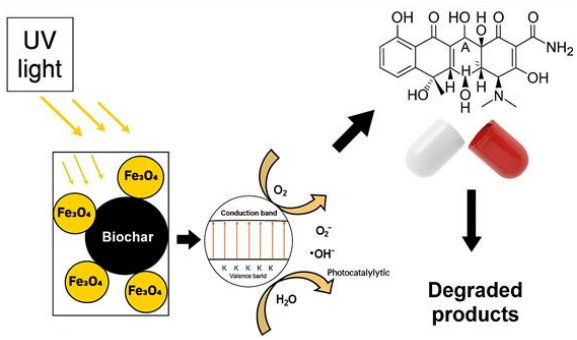


**Fig. 7.** Reaction mechanisms for the degradation of OTC

BC-Fe3O4 NPs + *hv*(UV) → BC-Fe3O4 NPs (e−(CB) + h+(VB))

H2O+ h+(VB) → OH˙ + H+

(O2−).O2 + e−(CB) → O2−˙

(OH˙).O2−˙+ H+ ⇄ HOO˙

2HOO˙ → H2O2+ O2

H2O2→ 2OH˙

+ OH˙ → CO2 + H2O (Antibiotics intermediates)

OTC + h+(VB) → oxidation products

OTC + e−(CB) → reduction products

OTC + *hv* → OTC*

OTC* + BC-Fe3O4 NPs → OTC+ BC-Fe3O4 NPs −

**OTC**

The main absorbance peaks of OTC appear between 200–400 nm, with distinct maxima around 275 nm and 360 nm. Over time, a reduction in absorbance reflects the progressive degradation of OTC. The control sample exhibits the highest absorbance, confirming that no degradation occurs in the absence of treatment. In contrast, after 60 minutes of exposure to BC-Fe3O4, a substantial decrease in absorbance is observed, indicating effective OTC removal likely driven by photocatalytic activity. The BC-Fe3O4 sample alone displays minimal absorbance, with a minor peak near 240 nm and an almost flat spectrum beyond 300 nm, suggesting it has negligible intrinsic absorbance and does not interfere with OTC detection. These UV-Vis results demonstrate that BC-Fe3O4 enables time-dependent degradation of OTC, achieving approximately 90% degradation after 60 minutes (Peiris *et al.*, 2017).

In Fig. 8 relatively linear degradation trend further supports the effectiveness of BC-Fe3O4 as a photocatalyst for OTC removal.

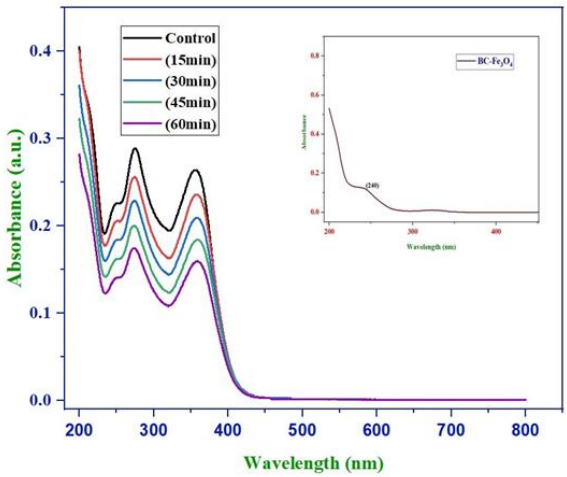


**Fig. 8.** UV-Visible spectra of BC-Fe3O4 nanoparticles (NPs)

The dosage percentage increases over time for all three dosages. Among them, the 0.5 g dosage consistently exhibits Fig. 9 the highest percentage, reaching nearly 90% at 60 minutes. The 0.05 g dosage follows, achieving around 85%, while the 0.005 g dosage shows the lowest performance at approximately 80% after 60 minutes. These results indicate that the efficiency of BC-Fe3O4 improves with increasing dosage, with the 0.5 g dosage being the most effective in reaching a higher dosage percentage within the 60-minute time frame (Danner *et al.*, 2019).

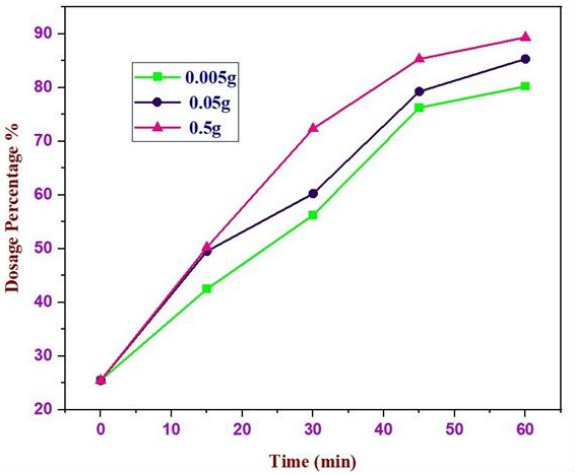


**Fig. 9**. Maximum amount of antibiotics degradation of model antibiotics at different dosage with time

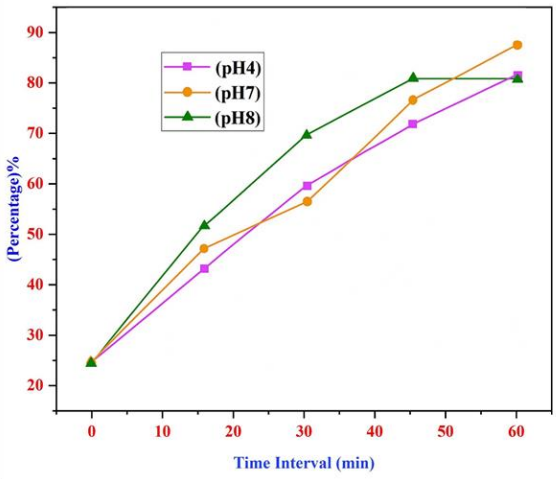


**Fig. 10.** Maximum amount of antibiotics degradation of model antibiotics at different pH with time

**pH with time**

Fig. 10 illustrates the percentage increase over time at different pH levels (pH 4, pH 7, and pH 8) for BC-Fe3O4, likely reflecting its adsorption efficiency or degradation rate.

At pH 4, there is a steady increase, reaching approximately 83% at 60 minutes. At pH 7, performance slightly surpasses that of pH 4 after 40 minutes, achieving the highest overall efficiency of around 88% at 60 minutes. pH 8 shows the fastest initial increase, reaching about 70% within 30 minutes, but plateaus around 80% after 45 minutes. This suggests that pH 8 provides the quickest initial reaction or adsorption rate, while pH 7 offers the best overall performance. Although pH 4 starts off with the slowest rate, it nearly matches pH 8 by the end of the experiment (Felis *et al.,* 2020). Overall, pH 7 is optimal for BC-Fe3O4, pH 8 yields the fastest initial response, and pH 4 is the least efficient, though its performance improves over time.

**Antibacterial activity**

BC-Fe3O4 exhibits the highest antibacterial activity within the first 15 minutes to 2 hours of exposure, showing inhibition zones between approximately 21% and 24%. Activity is moderate during this early period but significantly declines at 12 and 48 hours, indicating a time-sensitive release profile with peak efficacy shortly after administration. Among the tested bacteria, *E. coli* and *Serratia marcescens* are the most sensitive, showing the greatest inhibition, while *Klebsiella pneumoniae* and *Bacillus subtilis* exhibit lower sensitivity, particularly at extended exposure times. *Staphylococcus aureus* displays a consistent decline in response, highlighting reduced antibacterial efficacy over time. Overall, Fig. 11 the findings suggest that BC-Fe3O4 loaded with OTC provides time-dependent antibacterial activity, with rapid release and short-term exposure (within 2 hours) being critical for optimal performance (Wang *et al.,* 2019). Future formulations may benefit from strategies to prolong drug release or enhance stability for sustained antibacterial effects.

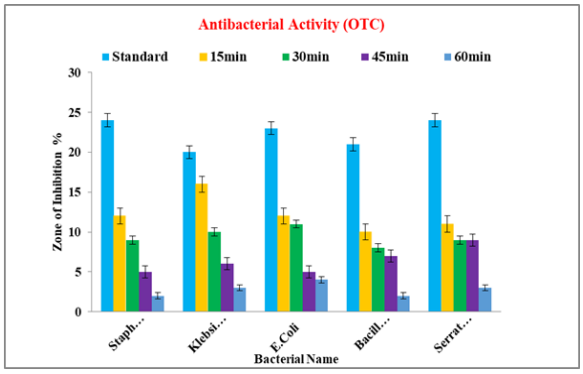


**Fig. 11.** BC-Fe3O4 -Oxytetracycline antibacterial activity

**Regeneration and reusability of BC-Fe3O4**

BC-Fe3O4 illustrates the regeneration efficiency of BC-Fe3O4 over three cycles at two dosages: 0.5g/50ml and 0.05g/50ml.In the first cycle, both dosages demonstrate high regeneration efficiencies (above 80%), with the 0.05g/50ml dosage Fig. 12 showing slightly better performance. By the second cycle, regeneration efficiency declines for both dosages, falling to approximately 60–62%, indicating a reduction in the material's regenerative capacity. In the third cycle, the 0.05g/50ml dosage continues to outperform the 0.5g/50ml dosage slightly, maintaining around 68% efficiency compared to 62%. Overall, the data suggests that BC-Fe3O4 retains moderate regeneration efficiency over three cycles, though performance diminishes with each use. The lower dosage (0.05g/50ml) consistently yields slightly better results, implying it may be

more effective or sustainable for repeated regeneration (Shakoor *et al.,* 2020).

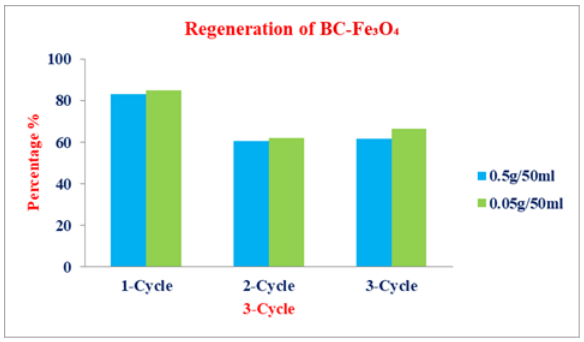


**Fig. 12.** Recyclability study of BC-Fe3O4

## CONCLUSION

This study successfully demonstrated the green synthesis of biochar-coated iron oxide nanoparticles (BC-Fe3O4 NPs) using *Miscanthus sinensis* for the efficient removal of oxytetracycline (OTC) from water. The synthesized nanocomposites exhibited favorable physicochemical characteristics- such as increased surface area, mesoporosity, and functional group modifications—confirmed through XRD, FTIR, SEM-EDX, TGA-DTA, and BET analyses. Photocatalytic experiments showed a notable OTC degradation efficiency of up to 49% within 60 minutes under UV light, with optimal results observed at neutral pH and higher nanoparticle dosages. Furthermore, BC-Fe3O4 NPs displayed time-dependent antibacterial activity, particularly against *E. coli* and *S. marcescens*, and maintained moderate regeneration efficiency over three reuse cycles. In conclusion, BC-Fe3O4 NPs represent a promising and environmentally friendly material for wastewater treatment and environmental remediation.

## ACKNOWLEDGEMENTS

Authors thank the Service of the instruments of the Manonmaniam Sundaranar University, Alwarkurichi and Periyar University for the SEM-EDS, FTIR, TGA images. Sharmila M. Research Scholar (Register No: 22114012052014) acknowledges the Research centre, Sri Paramakalyani Centre of Excellence in Environmental Sciences, Manonmaniam Sundaranar University, Alwarkurichi, for providing the support for this research work.

## REFERENCES

**Abruzzo A, Zuccheri G, Belluti F, Provenzano S, Verardi L, Bigucci F, Cerchiara T, Luppi B, Calonghi N.** 2016. Chitosan nanoparticles for lipophilic anticancer drug delivery: Development, characterization and *in vitro* studies on HT29 cancer cells. Colloids and Surfaces B: Biointerfaces **145**, 362-372.

**Ahmaruzzaman M.** 2021. Biochar based nanocomposites for photocatalytic degradation of emerging organic pollutants from water and wastewater. Materials Research Bulletin **140**, 111262.

**Akhtar MJ, Ahamed M, Alhadlaq HA, Alrokayan SA, Kumar S.** 2014. Targeted anticancer therapy: overexpressed receptors and nanotechnology. Clinica Chimica Acta **436**, 78–92.

**Chen JW, Wu QH, Rowley DC, Al-Kareef AMQ, Wang H.** 2015. Anticancer agent-based marine natural products and related compounds. Journal of Asian Natural Products Research **17**(2), 199–216.

**Danner MC, Robertson A, Behrends V, Reiss J.** 2019. Antibiotics pollution in surface fresh waters: Occurrence and effects. Science of the Total Environment **664**, 793–804.

**Dhila HH, Bhapkar AR, Bhame S.** 2025. Metal oxide/biochar hybrid nanocomposites for adsorption and photocatalytic degradation of textile dye effluents: A review. Desalination and Water Treatment **21**(3), 101004.

**El-Abid H, Amaral C, Cunha SC, Correia-da-Silva G, Fernandes JO, Moumni M, Teixeira N.** 2023. Anti-cancer properties of hydroethanolic extracts of *Juniperus oxycedrus* L. in breast cancer cells. Journal of Herbal Medicine **37**, 100614.

**Felis E, Kalka J, Sochacki A, Kowalska K, Bajkacz S, Harnisz M, Korzeniewska E.** 2020. Antimicrobial pharmaceuticals in the aquatic environment-occurrence and environmental implications. European Journal of Pharmacology **866**, 172813.

**Hazrati S, Farahbakhsh M, Cerdà A, Heydarpoor G.** 2021. Functionalization of ultrasound enhanced sewage sludge-derived biochar: Physicochemical improvement and its effects on soil enzyme activities and heavy metals availability. Chemosphere **269**, 128767.

**Hosny M, Fawzy M, Eltaweil AS.** 2022. Green synthesis of bimetallic Ag/ZnO Biochar nanocomposite for photocatalytic degradation of tetracycline, antibacterial and antioxidant activities. Scientific Reports **12**(1), 7316.

**Huang S, Zhu F, Qiu H, Xiao Q, Zhou Q, Su W, Hu B.** 2014. A sensitive quantum dots-based fluorescent sensor for ruthenium anticancer drugs and ctDNA. Colloids and Surfaces B: Biointerfaces **117**, 240–247.

**Jin YH, Cai L, Cheng ZS, Cheng H, Deng T, Fan YP, Fang C.** 2020. A rapid advice guideline for the diagnosis and treatment of 2019 novel coronavirus (2019-nCoV) infected pneumonia (standard version). Military Medical Research **7**(1), 1–23.

**Kumar SM, Liu S, Lu H, Zhang H, Zhang PJ, Gimotty PA, Guerra M, Guo W, Xu X.** 2012. Acquired cancer stem cell phenotypes through Oct4-mediated dedifferentiation. Oncogene **31**(47), 4898–4911.

**Li L, Ozden A, Guo S, García de Arquer FP, Wang C, Zhang M, Zhong M.** 2021. Stable, active $CO_2$ reduction to formate via redox-modulated stabilization of active sites. Nature Communications **12**(1), 5223.

**Mou Q, Ma Y, Zhu X, Yan D.** 2016. A small molecule nanodrug consisting of amphiphilic targeting ligand–chemotherapy drug conjugate for targeted cancer therapy. Journal of Controlled Release **230**, 34–44.

**Ntoutoume GMA, Granet R, Mbakidi JP, Brégier F, Léger DY, Fidanzi-Dugas C, Lequart V.** 2016. Development of curcumin-cyclodextrin/cellulose nanocrystals complexes: New anticancer drug delivery systems. Bioorganic & Medicinal Chemistry Letters **26**(3), 941–945.

**Oleszczuk K, Giwercman A, Bungum M.** 2016. Sperm chromatin structure assay in prediction of in vitro fertilization outcome. Andrology **4**(2), 290-296.

**Omer AM, Abd El-Monaem EM, Abd El-Latif MM, El-Subruiti GM, Eltaweil AS.** 2021. Facile fabrication of novel magnetic ZIF-67 MOF@aminated chitosan composite beads for the adsorptive removal of Cr(VI) from aqueous solutions. Carbohydrate Polymers **265**, 118084.

**Omer AM, Dey R, Eltaweil AS, Abd El-Monaem EM, Ziora ZM.** 2022. Insights into recent advances of chitosan-based adsorbents for sustainable removal of heavy metals and anions. Arabian Journal of Chemistry **15**(2), 103543.

**Pap S, Shearer L, Gibb SW.** 2023. Effective removal of metformin from water using an iron-biochar composite: Mechanistic studies and performance optimisation. Journal of Environmental Chemical Engineering **11**(5), 110360.

**Pathy A, Pokharel P, Chen X, Balasubramanian P, Chang SX.** 2023. Activation methods increase biochar's potential for heavy-metal adsorption and environmental remediation: A global meta-analysis. Science of The Total Environment **865**, 161252.

**Peiris C, Gunatilake SR, Mlsna TE, Mohan D, Vithanage M.** 2017. Biochar based removal of antibiotic sulfonamides and tetracyclines in aquatic environments: A critical review. Bioresource Technology **259**, 150–159.

**Salim AA, Bakhtiar H, Dawood DA, Ghoshal SK.** 2023. Anticancer and cytotoxicity evaluation of silver-cinnamon nanoshells. Materials Letters **334**, 133671.

**Saraswathy M, Gong S.** 2014. Recent developments in the co-delivery of siRNA and small molecule anticancer drugs for cancer treatment. Materials Today **17**(6), 298–306.

**Shafiq M, Ahmad A, Latif K, Saeed M, Ahmed I, Hyder MZ.** 2025. Prevalence of New Delhi Metallo-β-lactamase (bla NDM) gene in a selected population of drug-resistant clinical isolates. Molecular Biology Reports **52**(1), 388.

**Shafiq M, Ahmad A, Latif K, Saeed M, Ahmed I, Hyder MZ.** 2025. Prevalence of New Delhi Metallo-β-lactamase (bla NDM) gene in a selected population of drug-resistant clinical isolates. Molecular Biology Reports **52**(1), 388.

**Shakoor MB, Ali S, Rizwan M, Abbas F, Bibi I, Riaz M, Khalil U, Niazi NK, Rinklebe J.** 2020. A review of biochar-based sorbents for separation of heavy metals from water. International Journal of Phytoremediation **22**(2), 111–126.

**Shui J, Lin Y, Connell JW, Xu J, Fan X, Dai L.** 2016. Nitrogen-doped holey graphene for high-performance rechargeable Li–$O_2$ batteries. ACS Energy Letters **1**(1), 260–265.

**Tang J, Zhu W, Kookana R, Katayama A.** 2013. Characteristics of biochar and its application in remediation of contaminated soil. Journal of Bioscience and Bioengineering **116**(6), 653–659.

**Wang J, Wang S.** 2019. Preparation, modification and environmental application of biochar: A review. Journal of Cleaner Production **227**, 1002–1022.

**Xie YJ, Huang M, Li D, Hou JC, Liang HH, Nasim AA, Huang JM, Xie C, Leung ELH, Fan XX.** 2022. Bacteria-based nanodrug for anticancer therapy. Pharmacological Research **182**, 106282.

**Zhang Y, Qin L, Zhao Y, Zhang P, Xu B, Li K, Liang L.** 2020. Interferon-induced transmembrane protein 3 genetic variant rs12252-C associated with disease severity in coronavirus disease 2019. The Journal of Infectious Diseases **222**(1), 34–37.